UNIVERSITY OF HELSINKI REPORT SERIES IN PHYSICS

HU-P-D233

INELASTIC X-RAY SCATTERING SPECTROSCOPY OF SMALL MOLECULES AND THEIR RADIATION CHEMISTRY

Juho Inkinen

Division of Materials Physics
Department of Physics
Faculty of Science
University of Helsinki
Helsinki, Finland

ACADEMIC DISSERTATION

To be presented, with the permission of the Faculty of Science of the University of Helsinki, for public criticism in auditorium B123, Exactum, Gustaf Hällströmin katu 2B, on 19th of February 2016 at 12:15.

Helsinki 2016

Supervisors

Prof. Keijo Hämäläinen
Department of Physics
University of Helsinki
Helsinki, Finland

Dr. Simo Huotari
Department of Physics
University of Helsinki
Helsinki, Finland

Dr. Johannes Niskanen
Department of Physics
University of Helsinki
Helsinki, Finland

Pre-examiners

Prof. Adam P. Hitchcock
Department of Chemistry
McMaster University
Hamilton, Ontario, Canada

Dr. Jean-Pascal Rueff
SOLEIL Synchrotron
Saint-Aubin, France

Opponent

Prof. Jan-Erik Rubensson
Department of Physics and Astronomy
Uppsala University
Uppsala, Sweden

Custos

Prof. Keijo Hämäläinen
Department of Physics
University of Helsinki
Helsinki, Finland

Report Series in Physics HU-P-D233
ISSN 0356-0961
ISBN 978-951-51-1568-3 (printed version)
Picaset Oy
ISBN 978-951-51-1569-0 (pdf version)
http://ethesis.helsinki.fi/
Helsingin yliopiston verkkojulkaisut
Helsinki 2016

Preface

The work for this thesis has been carried out at the Department of Physics of the University of Helsinki. I am thankful to the current and previous head of the department, Prof. Hannu Koskinen and Prof. Juhani Keinonen, for the opportunity to work there. I acknowledge the Vilho, Yrjö, and Kalle Väisälä Foundation and the Academy of Finland for the financial support for this thesis. The European Synchrotron Radiation Facility is acknowledged for the opportunity to perform experiments with the facility's instruments.

I am deeply grateful to my three supervisors, whose expertise I respect greatly. They have had different roles in guiding me in my studies while each has been irreplaceable. First of all, I thank Prof. Keijo Hämäläinen for initially recruiting me to the x-ray laboratory and the HELIXS group. Especially I would like to mention his extraordinary ability to inspire and pass his own enthusiasm even in the shortest conversations. To Dr. Simo Huotari I am forever in debt for the enormous amount of help he has given me and for his endless patience. At the difficult times during my studies he has made me to continue and to look things from a brighter perspective. Also Dr. Johannes Niskanen I thank most warmly for his invaluable help and encouragement, especially for the hands-on assistance in getting manuscripts ready. It is fair to say he has saved the day innumerable times.

I would like to express my gratitude also to all other members of the x-ray laboratory and my co-authors. In particular, I thank Drs. Arto Sakko and Christoph Sahle, with whom I have had the pleasure to work and share exciting moments at a beamline. Also, I wish to thank Dr. Mikko Hakala for his support and Dr. Szabolcs Galambosi for his advice at early stages of this work. I am especially thankful to the office mates in "kulmahuone" for their good company during these years. Finally, I thank my friends for many pleasant moments of playing board games, traveling, bicycling, etc.; and my parents for their understanding when I have been too much away.

J. Inkinen: Inelastic X-ray scattering spectroscopy of small molecules and their radiation chemistry, University of Helsinki, 2016, 42 pages + appendices. University of Helsinki, Report Series in Physics, HU-P-D233.

Keywords: inelastic x-ray scattering, x-ray Raman scattering, synchrotron radiation, molecular spectroscopy, molecular vibrations, x-ray induced reactions

Abstract

Non-resonant inelastic x-ray scattering can provide information on various atomic-scale properties and phenomena by probing the spectrum of electronic excitations. The technique allows bulk-sensitive measurements and relatively freely tunable sample conditions even for excitations with energies in the soft x-ray range. Also non-dipolar excitations are accessible by virtue of the ability to impose finite momentum transfer in the scattering process. This thesis comprises of studies that apply non-resonant inelastic x-ray scattering to questions of chemistry and physics in gas and solid phase. More specifically, the works focus on selected cases of gas-phase samples at elevated temperatures and pressures as well as on a solid-state chemical reaction of an organic compound.

The electronic excitation spectra from gas-phase molecules exhibit temperature dependence due to molecular vibrations, which affect both the intensities and energies of the electronic transitions. The spectra measured at varied sample temperature and with varied momentum transfer help to give insight to the vibrational effects when interpreted using spectrum simulations. Especially the vibrations that distort the molecular symmetry from that of the equilibrium geometry are demonstrated to be important.

A classic example of topochemical reactions is the dimerization of crystalline cinnamic acid, which is usually induced by ultraviolet light illumation. The presented study with inelastic x-ray scattering shows the reaction take place also due to x-ray irradiation. The in-situ measured time-resolved spectra allow to obtain reaction kinetics data, and the utilization of imaging method to follow also the spatial progress of the reaction.

These novel experiments using non-resonant inelastic x-ray scattering and the applied analysis methods demonstrate the versatility of the technique and help to envision future studies.

List of papers

This thesis consists of an introductory part and four research articles, which are referred to by the Roman numerals **I**–**IV** throughout the text.

I A. Sakko, S. Galambosi, **J. Inkinen**, T. Pylkkänen, M. Hakala, S. Huotari, and K. Hämäläinen. *Inelastic X-ray scattering and vibrational effects at the K-edges of gaseous N_2, N_2O, and CO_2.* Physical Chemistry Chemical Physics, **13**, 11678–11685 (2011).

II **J. Inkinen**, A. Sakko, K. O. Ruotsalainen, T. Pylkkänen, J. Niskanen, S. Galambosi, M. Hakala, G. Monaco, S. Huotari, and K. Hämäläinen. *Temperature dependence of CO_2 and N_2 core-electron excitation spectra at high pressure.* Physical Chemistry Chemical Physics, **15**, 9231–9238 (2013).

III **J. Inkinen**, J. Niskanen, A. Sakko, K. O. Ruotsalainen, T. Pylkkänen, S. Galambosi, M. Hakala, G. Monaco, K. Hämäläinen, and S. Huotari. *Interplay between Temperature-Activated Vibrations and Nondipolar Effects in the Valence Excitations of the CO_2 Molecule.* The Journal of Physical Chemistry A, **118**, 3288–3294 (2014).

IV **J. Inkinen**, J. Niskanen, T. Talka, Ch. J. Sahle, H. Müller, L. Khriachtchev, J. Hashemi, A. Akbari, M. Hakala, and S. Huotari. *X-ray induced dimerization of cinnamic acid: Time-resolved inelastic X-ray scattering study.* Scientific Reports, **5**, 15851 (2015).

The papers **I**–**IV** are included as appendices in the printed version of this thesis and they have been reproduced with permission from the publishers (for **I**–**II** the PCCP Owner Societies, for **III** the American Chemical Society, for **IV** the Nature Publishing Group).

Author's contribution

The author of this thesis wrote the first versions of papers **II**–**IV** except their sections concerning computations. In all papers he has been responsible for planning and conducting the experiments, which for papers **I**–**III** has included designing and assembling sample-environment setups and for paper **IV** preparing samples together with T.T. In papers **II**–**IV** he analyzed the data from the inelastic x-ray scattering experiments and contributed actively to the interpretation of the experimental and computational results.

Paper **I** has been previously included in the dissertation of Dr. Arto Sakko (Department of Physics, University of Helsinki, Helsinki 2011).

Related work

List of work by the author that is closely related to this thesis but not included in it:

1. Ch. J. Sahle, A. Mirone, J. Niskanen, **J. Inkinen**, M. Krisch, and S. Huotari. *Planning, performing and analyzing X-ray Raman scattering experiments.* J. Synchrotron Radiat. **22**, 400 (2015).

2. K. Ruotsalainen, **J. Inkinen**, T. Pylkkänen, T. Buslaps, K. Hämäläinen, M. Hakala, and S. Huotari. *The isotropic Compton profile difference across the phase transition of* VO_2. Submitted to J. Phys. Chem. Solids.

Contents

1 Introduction

The development of experimental techniques is an important driving force behind many advances of physics. Among the most rapidly developed techniques are those based on synchrotron radiation, which has in many ways revolutionized materials science. The advances in the instrumentation at synchrotron radiation facilities have made new techniques feasible, non-resonant inelastic x-ray scattering (NRIXS) spectroscopy being one of them. In the NRIXS process some of the energy and momentum of an incident x-ray photon is transferred to a sample system that is excited to a higher-energy state [1]. This probing of excited electronic states yields information on the properties of the sample material on atomic level.

The most remarkable feature of NRIXS is its versatility and applicability to various samples and sample conditions. This gives the technique value as a complementary method to similar spectroscopies, which are far more restricting in this regard. NRIXS from core-electrons is called x-ray Raman scattering (XRS). For measuring core-level spectra from light elements (e.g., C, N, O) XRS enables to probe the interior of macroscopic-scale samples [1–3] as well as to use elaborate sample cells for readily tunable, non-vacuum, and even extreme sample conditions [4]. Another important feature of NRIXS is its ability to probe also non-dipolar excitations, which enables gaining a more complete description of electronic structures [5–7]. In terms of applications, suitable instrumentation dedicated for NRIXS can be used to spectroscopic tomography [8], which enables to spatially map chemical bonding inside a sample [9].

This thesis focuses on novel NRIXS studies on molecular chemistry and physics. The NRIXS technique has become feasible comparatively recently, and it is still rapidly developing and enables novel experiments to be performed [9–11]. Also the amount of data produced in the measurements has increased significantly, presenting challenges for data analysis and raising questions on the most efficient ways to use the data.

First, in Section 2, the background of NRIXS is briefly presented. In Section 3 the studied phenomena, i.e., molecular vibrations and radiation induced chemical reactions, are discussed. Section 4 presents experimental aspects including instrumentation and methods for data analysis, tomographic imaging, and spectrum interpretation. Section 5 describes the experiments performed for papers **I**–**IV**. In papers **I**–**III** electron-excitation spectra of gas-phase molecules were studied, the interest lying in the effects of molecular vibrations, their temperature dependence (papers **II**–**III**), and non-dipole excitations (papers **I**,**III**). In paper **IV** NRIXS was used to study dimerization of cinnamic acid to truxillic acid, which is a classic example of a topochemical solid-state reaction. The progress of this reaction was followed by time-resolved imaging of the sample crystal, and the reaction kinetics was investigated using spectral decomposition.

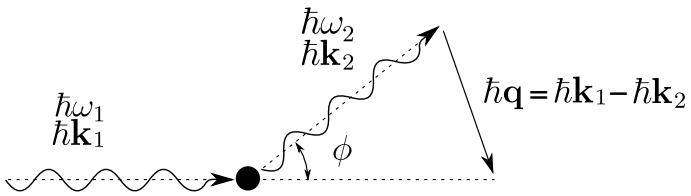

Figure 1: Schematic presentation of inelastic x-ray scattering.

2 Non-resonant inelastic x-ray scattering

An interaction between x-rays and matter can be described by a cross-section σ, which is defined for an atom or molecule as the rate of the interaction events divided by the density of incident photon flux (photons per unit time per unit area) [12, 13]. In the case of inelastic x-ray scattering interaction, both momentum and energy of the incident and scattered photons differ. In an inelastic x-ray scattering experiment the photons scattered to a solid-angle element $\mathrm{d}\Omega$ in an energy bandwidth $\mathrm{d}\hbar\omega_2$ are detected, and the measured quantity is a double differential cross section (DDCS) [1]. When the energy of the incident x-rays is far from the absorption edges of the electronic system, the dominant contribution to the DDCS is given by non-resonant inelastic x-ray scattering (NRIXS) [3]. This process arises from the $\mathbf{A} \cdot \mathbf{A}$ term in the interaction Hamiltonian of the electromagnetic radiation and the electronic system, $\mathbf{A}$ being the vector potential of the radiation field.

The DDCS for NRIXS can be written as

$$\frac{\mathrm{d}^2\sigma}{\mathrm{d}\Omega \mathrm{d}\omega_2} = \left(\frac{\mathrm{d}\sigma}{\mathrm{d}\Omega}\right)_{\mathrm{Th}} S(\mathbf{q}, \omega). \tag{1}$$

Here, the first factor is the Thomson cross section [13], which reads

$$\left(\frac{\mathrm{d}\sigma}{\mathrm{d}\Omega}\right)_{\mathrm{Th}} = r_0^2 \frac{\omega_2}{\omega_1} |\hat{\mathbf{e}}_1 \cdot \hat{\mathbf{e}}_2^*|^2. \tag{2}$$

The Thomson cross section formula includes the classical electron radius r_0, the energies of the incoming and scattered photons $\hbar\omega_1$ and $\hbar\omega_2$, and their polarization vectors $\hat{\mathbf{e}}_1$ and $\hat{\mathbf{e}}_2$, respectively.

The second part in Eq. (1) is the dynamic structure factor of the electronic system,

$$S(\mathbf{q}, \omega) = \sum_{F,I} \rho_I \left| \langle F | \sum_j \mathrm{e}^{i\mathbf{q}\cdot\mathbf{r}_j} | I \rangle \right|^2 \delta(E_F - E_I - \hbar\omega). \tag{3}$$

In this form, the dynamic structure factor describes transitions from the initial states $|I\rangle$ to final states $|F\rangle$, which have energies E_I and E_F, respectively. The probability of the initial state $|I\rangle$ to be occupied is ρ_I. The energy transfer to the electronic system is $\hbar\omega = \hbar\omega_1 - \hbar\omega_2$ and momentum transfer is $\hbar\mathbf{q} = \hbar\mathbf{k}_1 - \hbar\mathbf{k}_2$. The summation index

j runs over all electrons in the system, and the delta function forces the conservation of energy.

As depicted in Fig. 1, the scattering vector $\mathbf{q}$ is set in an NRIXS experiment by the scattering angle ϕ together with the photon momenta. The magnitude of the scattering vector is

$$q = \frac{1}{c}\sqrt{\omega_1^2 + \omega_2^2 - 2\omega_1\omega_2 \cos\phi}, \tag{4}$$

where c is the speed of light. The dynamic structure factor depends on the momentum transfer via the exponential operator in Eq. (3), which can be expanded as a series of Cartesian operators:

$$\mathrm{e}^{i\mathbf{q}\cdot\mathbf{r}} = 1 + i\mathbf{q}\cdot\mathbf{r} - \frac{1}{2}(\mathbf{q}\cdot\mathbf{r})^2 + O(q^3). \tag{5}$$

In the limit $q \to 0$, the dynamic structure factor is governed by the second term of the series that gives rise to dipole transitions. With increasing momentum transfer, higher-order terms gain significance, and this presents a way to probe also non-dipole excitations and to obtain a more complete picture of the electronic system [1, 5].

At energy transfer values close to electron binding energies the dynamic structure factor of an electronic system exhibits thresholds that correspond to absorption edges. The spectral near-edge features just below the thresholds consist of excitations to bound electronic states, which in isolated molecules are described by molecular orbitals [12,14]. The cases of core and valence electron excitations are discussed in the next two sections along with the relation of NRIXS to similar techniques.

Figure 2 shows an NRIXS spectrum on a wide energy transfer range measured from liquid acetic acid with several momentum transfer values. The regions of carbon and oxygen K-edges are shown enlarged in the insets. The valence-electron excitations form a broad profile, whose maximum shifts to higher energy transfer values with increasing q, and which appears as a background for the core-electron excitations. By increasing q to be much larger than the inverse of the characteristic interparticle distances, the dynamic structure factor takes the form of Compton profile [15], which in non-relativistic limit is centered at the energy transfer $\hbar^2q^2/2m$, m being the electron mass.

2.1 X-ray Raman scattering

The term X-ray Raman scattering (XRS) for NRIXS from core electrons is due to its analogy with (ordinary) Raman scattering [16]. The near-edge features in a core-electron excitation spectrum are sensitive to the chemical bonds and local molecular structure around the excited atom site.[1] The edges of different elements are well separated from each other, which enables element-specific measurements. However, the

[1]The spectrum region around an absorption edge is customarily termed XANES for x-ray absorption near edge structure or NEXAFS for near edge x-ray absorption fine structure.

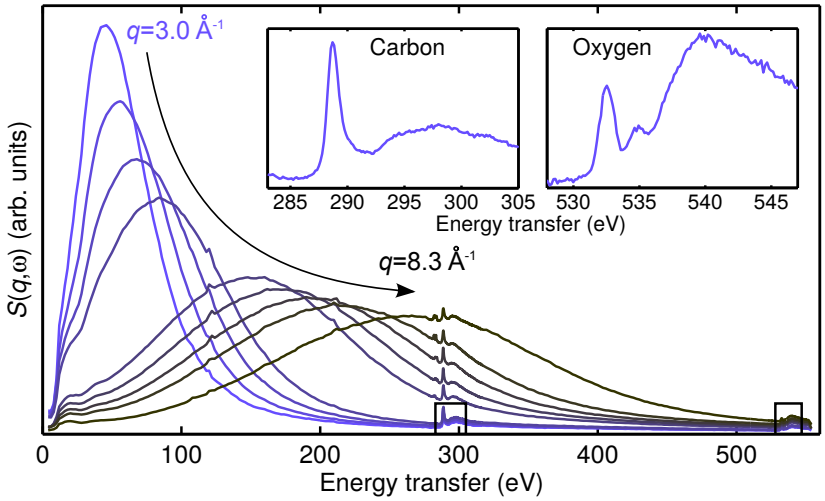

Figure 2: NRIXS spectra from liquid acetic acid ($C_2H_4O_2$) for $q = 3.0 - 8.3$ Å^{-1}. The carbon and oxygen near-edge regions for $q = 3.0$ Å^{-1} are shown enlarged in the insets.

relation between the molecular structure and the spectral features is not straightforward, and the spectrum interpretation relies largely on simulations [17–21]. Depending on the modeled electronic system, various effects need to be accounted for by the simulation. For example, in the case of gas-phase molecules, spectral effects appear due to molecular vibrations, studied in papers **I**–**III**, and discussed in Section 3.1.

The core-electron absorption edges of light elements are in the energy range of soft x-rays (below 1 keV for $Z<10$). However, because in XRS the energy transfer takes the role of incident-photon energy in absorption process, even high-energy x-rays can be used to probe these energy ranges. When the energy of incident x-rays is around 10 keV, their probing depth is in mm-range in materials that consist of light elements. Thus, the XRS measurements of low-Z elements are bulk-sensitive in a macroscopic length scale and enable the use of elaborate sample environments. Vacuum conditions are not necessary and it is even possible to use sample cells that allow readily tunable pressure and temperature. Even extreme pressures can be realized in XRS experiments by using a diamond anvil cell [4, 22–27].

2.2 Complementary techniques

The more widely used techniques for measuring core-electron excitations are x-ray absorption and electron energy loss spectroscopy (XAS and EELS, respectively). XAS is based on the measurement of photoabsorption cross section [12], which is mainly governed by dipole transitions: $\sigma_{\mathrm{abs}} \propto |\hat{\mathbf{e}}_1 \cdot \langle F|\mathbf{r}|I\rangle|^2$. Thus, XAS and XRS in the limit of low q yield equivalent information. The direction of the momentum transfer in XRS has the role that the polarization of the x-rays has in absorption as seen from Eq. (5).

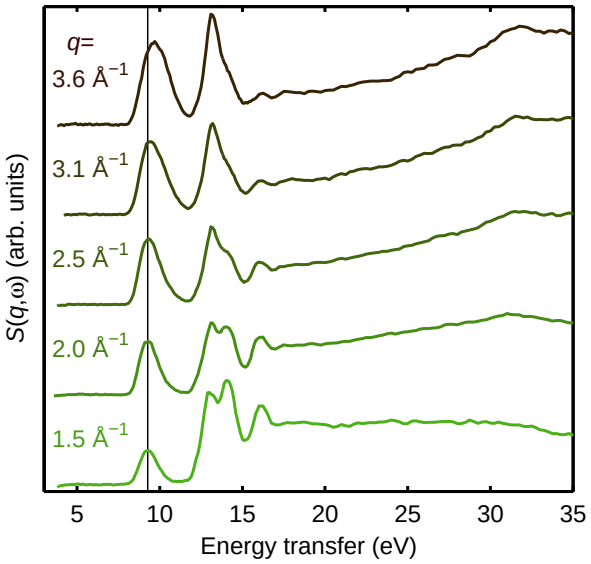

Figure 3: NRIXS spectra of valence-electron excitations from gaseous N_2 showing dependence on the momentum transfer. The spectra are offset for clarity. The vertical line emphasizes the shift of the lowest-energy peak.

When the interest is in low-energy excitations (<1 keV), the probing depth in XAS is small in solid and liquid samples (in the range of ∼1 µm) [28].

EELS is more analogous to XRS, in the sense that also it aims in measuring the dynamic structure factor and allows to probe non-dipole excitations [29]. However, as electron scattering arises from the Coulomb interaction, the cross section that EELS measures is relatively large and it decreases with increasing momentum transfer [30]. For this reason EELS measurements can be complicated by multiple scattering that can render the measured spectrum not to correspond to the dynamic structure factor. Recent comparative studies with EELS and NRIXS [31–36] have shown that multiple scattering can affect EELS spectra even when measured using high-energy electrons and that it can arise also from an intramolecular process. Similar restrictions for probing depth as for XAS concern also EELS. A valuable advantage with EELS, owing to the electron beam focusing possibility, is the ability to perform spatially resolved measurements with nm-scale resolution [37].

In this thesis XRS was chosen as the superior technique for the presented studies, since it allows for well-defined beyond-ambient thermodynamic conditions as well as hyperspectral imaging over macroscopic length scales.

2.3 Valence excitations

The electrons that occupy valence orbitals have low binding energies, and their excitations are usually studied by UV-visible light absorption spectroscopy [16] or by EELS. Generally, the valence-excitation spectrum does not offer element specificity unlike core-excitation spectrum does, but it can yield information on specific groups of atoms (chromophores) in molecules. UV-visible spectroscopy is the basis for many analytical methods in chemistry to identify compounds and determine concentrations [38]. The

valence-electron excitations themselves are interesting because they govern the optical properties of materials such as refraction and absorption [30]. Photochemical reactions are initiated by valence-electron excitations, which makes them relevant to, e.g., atmospheric chemistry [39, 40] and photosynthesis [41].

UV-visible light spectroscopy probes dipole excitations, and again here NRIXS excels by offering an access to non-dipolar transitions as well. This is illustrated in Fig. 3, which presents the q-dependent spectra from gas-phase N_2. The lowest-energy feature at 8–11 eV arises from two individual dipole-forbidden transitions [32]. Their behavior as a function of q are slightly different from each other, and this results in a blue shift of the unresolved double peak with increasing q.

3 Studied phenomena

3.1 Molecular vibrations and temperature

The electronic excitation spectrum of gas-phase molecules exhibits vibrational effects and generally also temperature dependence. When the electronic state of a molecule changes, also the potential energy surface (PES) governing the nuclei motion changes (Fig. 4). This results in vibrational excitations that accompany the electronic excitation, i.e., vibronic excitations [14, 16]. The initial population of the vibrational states depends on temperature, whose changes, in turn, are expected to give rise to spectral variations. The vibronic excitations provide a way to investigate the PES of both ground and excited electronic states, and temperature-varied spectra can help to probe them [42–45]. However, sophisticated computational methods are needed for any realistic simulation of the spectra to account accurately both electronic and vibrational effects [46–52]. If the individual vibrational side-peaks are not resolved in the spectrum, they appear as (generally asymmetrical) broadening of the electronic excitation features. From the point of view of applications, high-temperature gases and their spectroscopic studies are relevant to, for example, chemical reactions like combustion and industrial synthesis processes [53, 54], and to the atmospheric chemistry of Earth and other planets [39, 40, 55, 56]. Molecules can also undergo vibrational-state specific chemical reactions [57], allowing to tune chemical processes by selectively exciting vibrational modes [58].

Vibrational effects on electronic excitation spectra of gas-phase molecules have been studied extensively with several techniques. Using XAS and EELS the spectra of core-excitations can be recorded with a very fine resolution. For example, the resolution of ∼30–70 meV in the studies of CO_2 [59–63] and N_2 [64–68] has allowed to reveal the vibrational fine structure of the spectra. Also many studies with UV absorption spectroscopy and EELS have been performed on the valence excitations of these molecules, e.g., refs. [69–76]. NRIXS experiments on gaseous samples have become feasible in recent years with the help of sample cells allowing pressure to be increased above atmospheric pressure, which counteracts the comparatively small cross-section of NRIXS. So far gases studied using NRIXS include He, Ne, Ar, N_2, and CO [11,31–35,77,78], in addition to N_2, CO_2, and N_2O studied in papers **I**–**III**. The high resolution (70 meV) in the measurements of N_2 and CO valence-excitation spectra has allowed resolving vibrational side-peaks and studying their individual q dependence [35, 36].

A typical quantum mechanical framework for molecular vibrations relies in the Born–Oppenheimer approximation [79, 80], in which the vibronic wavefunction is written as a product of an electronic wavefunction $\Phi(\mathbf{r};\mathbf{R})$ and a vibrational wavefunction $\chi(\mathbf{R})$. Here $\mathbf{r}$ denotes all electron coordinates and $\mathbf{R}$ the nuclear ones. For the initial and final vibronic states of an excitation process this factorization yields $|I\rangle = |\Phi_{Ie}\rangle|\chi_{Ie,Iv}\rangle$ and $|F\rangle = |\Phi_{Fe}\rangle|\chi_{Fe,Fv}\rangle$, respectively. It is customary to apply the

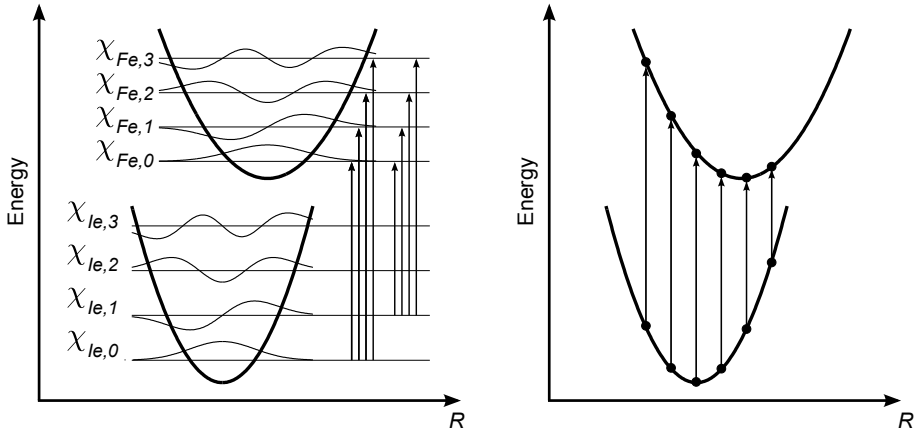

Figure 4: Schematic harmonic potential energy curves for initial and final electronic states with different equilibrium geometry and transitions following the Franck–Condon principle. Left: In the quantum mechanical framework the probability of a vibrational transition accompanying an electronic one depends on the overlap of the vibrational wavefunctions. Right: In the classical model an electronic excitation can be depicted as a vertical transition between the potential energy curves, as illustrated for a few geometries.

Franck–Condon principle, in which an unchanged molecular geometry during electronic transitions is assumed [16]. In this framework the dynamic structure factor (Eq. (3)) reads

$$S(\mathbf{q},\omega) = \sum_{Fe,Fv,Ie,Iv} \rho_{Ie,Iv} \Big| \langle \chi_{Fe,Fv} | \chi_{Ie,Iv} \rangle \, \langle \Phi_{Fe} | \sum_j \mathrm{e}^{i\mathbf{q}\cdot\mathbf{r}_j} | \Phi_{Ie} \rangle \Big|^2 \delta\big[(E_{Fe} - E_{Ie}) + (E_{Fv} - E_{Iv}) - \hbar\omega \big]. \tag{6}$$

The energy transfer now accounts for the energy difference of the electronic states, $E_{Fe} - E_{Ie}$, and that of the vibrational states, $E_{Fv} - E_{Iv}$. In the harmonic approximation, the contribution to the vibrational state energy by each normal mode is $\hbar\omega_M(n_M + 1/2)$, where ω_M is the vibrational angular frequency and n_M the vibrational quantum number of the mode M. The initial vibrational states are weighted with their temperature dependent statistical probabilities $\rho_{Ie,Iv}$. The vibrations are manifested in the electronic excitation spectrum as a fine structure: each electronic transition is accompanied by vibrational transitions, whose intensities are proportional to the square of the overlap integral of the vibrational wavefunctions (Franck–Condon factor). Figure 4 presents an illustration for a one-dimensional case. The vibrational wavefunctions are labelled $\chi_{Ie,n}$ and $\chi_{Fe,n}$, because they are determined by the PES of the electronic states Ie and Fe. For a given electronic state the vibrational wavefunctions are mutually orthogonal, but the PES of different electronic states are generally different, which allows multiple non-zero Franck–Condon factors for each electronic transition.

In many cases the Franck–Condon approximation in Eq. 6 is sufficient to explain

the vibrational fine structure of an electronic excitation spectrum. However, if the electronic transition moment is forbidden by selection rules, but it is accompanied by non-totally symmetric vibrational states, the overall vibronic transition can be allowed, since selection rules concern the full vibronic wavefunctions rather than solely their electronic part [16]. In case of forbidden electronic transition in the equilibrium geometry, expression of Eq. 6 is no more adequate, as the nuclear-coordinate dependence of the electronic transition moment can be important. This can be addressed by introducing correction terms from the series expansion of the electronic transition moment along normal coordinates. The first of them is the so-called Herzberg–Teller term, which includes derivatives of the electronic transition moment with respect to each normal coordinate, and these can be nonzero although the electronic transition moment is zero.

It is possible to treat the vibrations also in a classical framework, in which there are no quantized vibrational states. Instead, the nuclei of a molecule are treated as classical particles, whose motion is governed by the PES given by the electronic state. The vibrational effects arise as the electronic transitions are calculated for several molecular geometries and weighted with the probabilities of the geometries. This follows the Franck–Condon principle, as the transitions are vertical between the PES of the initial and final electronic state, and the transition energy is given by their energy difference, see Fig. 4. As in the quantum mechanical framework, the different shape of the PESs is necessary for vibrations to affect the spectrum, but now the effect is a continuous broadening of the peaks of the electronic transitions. In this model, the spectra depend on the temperature, because the probability distribution of the molecular geometries is governed by the vibrational energy. To model the transitions in this framework, the probability distribution of geometries can be sampled in the whole normal coordinate space, as in paper **II**, or only along one important normal coordinate, as in paper **III**.

3.2 Radiation-induced reactions

X-ray irradiation can induce chemical reactions in materials. Their consequences are called radiation damage, if they are undesired; however, in many fields of chemistry, the radiation or light-induced reactions are themselves important [81, 82]. Radiation damage has gained recently much interest in the fields of protein crystallography [83–86] and x-ray microscopy [87, 88], as it has become more important due to increased x-ray beam intensities. In crystallography, radiation damage is typically classified either as local damage (specific chemical changes), or as global damage of the whole crystal [84, 85]. The global damage includes the loss of crystalline order and changes in the unit cell dimensions. The underlying local damage, or intentionally induced chemical reaction, depends essentially on the specific chemical structure of the irradiated material [89].

The rate of the damage is governed naturally by the dose rate,[2] which can also affect the reaction pathway [81]. In gas-phase molecules it has been shown that even the specific ionized state affects the reaction path and disintegration products [90, 91].

The first step in all reaction pathways induced by x-rays is either photoelectric absorption or inelastic scattering, because they are the possible interactions that deposit energy to a material. In the case of atoms of elements $Z>3$ and $\hbar\omega_1 \approx 10$ keV, the dominant process is photoelectric absorption [92], which results in an ejected photoelectron and a singly-ionized state of the absorbing atom. Inelastic scattering that results in ionization of an atom produces both a scattered photon and an ejected Compton-electron. In the case of light elements ($Z<30$), a core-ionized state decays dominantly via the Auger process, in which an electron is emitted and the atom is left in a doubly ionized state [13]. In the case of heavier elements, core-ionized states decay dominantly by fluorescence process [92].

The released electrons cause subsequent secondary ionization and excitation events as well as bremsstrahlung in the material they propagate in, and the electrons from the secondary ionization events can themselves cause further processes [89]. The number of the excitations or ionizations produced by one high-energy electron can be large, which makes the interactions of the high-energy electrons more important for radiation damage than the initial x-ray interaction itself. Eventually, when the kinetic energy of the electrons is consumed, they can recombine with the ionized molecules to form electronically and/or vibrationally excited molecules, or seek to an electroaffinic site [85]. The chemical changes in a material begin most importantly from the valence-excited or ionized states created by the propagating electrons [89]. The free radicals that can be produced in the disintegration of molecules typically cause further reactions [93]. Generally, based on bond energies, it is expected that single carbon bonds are more sensitive to radiation than higher-order carbon bonds [94]. In turn, compounds containing an aromatic ring are found relatively radiation resistant [89]. In addition to molecule disintegration reactions combination processes are also known to occur [95–97], most importantly in polymers [82].

A general practice in x-ray experiments to reduce radiation damage is to cool the sample to cryogenic temperatures. This slows the migration of free radicals and the reactions they cause [86]. Naturally, the radiation dose can be decreased also by increasing the irradiated sample volume by increasing the x-ray beam size on the sample, which in turn decreases the fluence. In the experiment of paper **IV**, sample cooling and increased beam size were employed to decrease the rate of the x-ray-induced reactions. This enabled to follow the reactions with a time-resolved measurement.

Another experimental parameter that affects the radiation dose is the x-ray energy. The general behavior of photoelectric absorption cross-section as a function of energy is approximately $(\hbar\omega_1)^{-3}$, thus, for a fixed number of photons incident on a sample,

[2] The rate of energy deposited by radiation per unit mass.

the dose behaves as $(\hbar\omega_1)^{-2}$ (ignoring absorption edges) [92]. Considering NRIXS, the cross-section increases with an increasing incident-photon energy, which can further reduce the dose versus the measured signal. It is also possible to circumvent the effects of radiation damage by continuously refreshing the sample during a measurement. This approach is employed in, e.g., x-ray diffraction measurements with free-electron lasers by injecting sample crystals to the x-ray beam using a jet of carrier solution, or by translating a crystal between each exposure to probe an undamaged volume [98]. Similarly, in spectroscopic experiments on liquid samples radiation damage is commonly avoided by using a setup in which a circulation system continuously drives unirradiated sample volume into the x-ray beam [99, 100].

4 Experimental methods and considerations

4.1 General

In comparison to XAS and EELS, the NRIXS technique is characterized by the large probing depth of hard x-rays, and the small cross section of the NRIXS interaction itself [92]. Inelastic scattering is also diffuse, and only a fraction of the inelastically scattered photons can be detected.[3] Therefore, in NRIXS studies the spectral brightness of the x-ray source[4] needs to be high and the detection of scattered photons efficient. The use of high-energy x-rays (∼10 keV) also requires high instrumental resolving power. These simultaneous requirements are fulfilled by modern synchrotron radiation sources and beamlines specialized for NRIXS employing spectrometers with multiple analyzer crystals [8, 102, 103].

The required energy resolution depends on the probed excitations and the purpose of the experiment. In some experiments one may wish to resolve vibrational finestructure of an electronic-excitation spectrum, and the energy resolution must then match that of the difference of vibrational state energies. However, in many studies of electron excitations the requirement for energy resolution is dictated by the intrinsic spectral width that depends on the excited state lifetime; this is for example 130–180 meV for an oxygen 1s core hole [104].

In the case of low-density or dilute samples, the signal-to-noise ratio is an important factor considering the feasibility of experiments. A considerable background for the desired spectrum of core-electron excitations can arise from the valence-electron excitations of the sample itself. As seen in Fig. 2, the spectrum of the valence electrons (Compton profile) is centered at an energy transfer value that depends on the momentum transfer. This should be considered carefully when planning the experiments, in which the program package presented in ref. [105] can be used. Another factor that may affect the feasibility of an experiment is the radiation damage that the high intensity x-rays can cause in the sample, as discussed in Section 3.2.

The NRIXS experiments of this thesis have been carried on at the beamlines ID16 [8] (papers **I**–**III**) and ID20 (paper **IV**) of the European Synchrotron Radiation Facility (ESRF), located in Grenoble, France. The beamline ID20 opened for user experiments in 2013 replacing ID16. The main components and operation principles of ID16 were similar to those of ID20.

4.2 Synchrotron radiation sources and beamline ID20

A synchrotron radiation source is a particle accelerator dedicated to generating electromagnetic radiation for scientific experiments [13, 106]. In the storage ring of the ESRF

[3] At beamline ID20 the 72 analyzers cover 4.5% of the full 4π solid angle.

[4] Spectral brightness is defined as the number of photons/s/mm^2/mrad^2/(0.1% bandwidth) [101].

electrons circulate with an energy of 6 GeV. The electrons are steered by magnetic fields, and as charged particles under acceleration, they emit electromagnetic radiation. An undulator is a device positioned on a straight section of a storage ring for producing x-rays with high spectral brightness and with a tunable energy [13, 101]. An undulator consists of magnets arranged to produce a periodic magnetic field with alternating direction along its length, and the electrons that traverse it oscillate and emit synchrotron radiation. Due to coherent emission from different periods the undulator produces a radiation spectrum with a peaked structure consisting a fundamental energy and its harmonics [13, 101], which can be tuned by tuning the magnetic field strength (the gap of the magnets). The synchrotron radiation from an undulator is naturally concentrated to a narrow cone (i.e., x-ray beam), which is directed to a beamline. There can be several dozens of beamlines around a storage ring, each of them with different instrumentation dedicated to different experimental techniques.

At the beamline ID20 of ESRF the x-ray beam from the undulators is first narrowed using slits. Next, the beam is collimated with a mirror, and monochromatized with a premonochromator and a channel-cut monochromator. Their pass-energy, given by Bragg's law, is tuned simultaneously with the undulator gap to allow energy scanning. Finally, mirrors focus the x-ray beam to the sample position.

At ID20 the NRIXS spectrum is measured using the inverse energy scan technique, in which the intensity of the scattered x-rays at a constant energy is recorded, while changing the incident-photon energy to yield a desired energy-transfer range. This allows the use of a fixed-energy spectrometer, for which the efficiency remains constant throughout the energy scan, and the accessible energy range is limited by the monochromator and not the angle-dispersive spectrometer angular range. The NRIXS spectrometer of ID20 consists of six modules (three in vertical and three in horizontal scattering plane), whose scattering angle can be changed. Each module houses one two-dimensional spatially-sensitive detector and twelve spherically bent Si(110) analyzer crystals. The detectors have 256×256 pixels each of size 55×55 µm^2. The analyzer crystals serve two purposes: first, they energy-analyze the scattered radiation, i.e., they permit only radiation with a specific energy to be reflected to the detector [107]; secondly, owing to their spherical bending, they focus the reflected radiation in a point-to-point manner (sample-to-detector) [8]. The focusing property, when combined to the spatial sensitivity of the detector [108], enables imaging of the sample with contrast given by NRIXS — a novel spectroscopic tomography technique that is discussed in detail in Sec. 4.4.

In the studies of this work, the energy resolution was 0.5 eV in papers **I**–**III** and 0.7 eV in paper **IV**, which values were determined from the full width at half maximum of elastic line. When signals from multiple analyzer crystals are summed to obtain a single spectrum, the momentum transfer resolution is dictated via Eq. (4) by the range of the scattering angles that the crystal positions span.

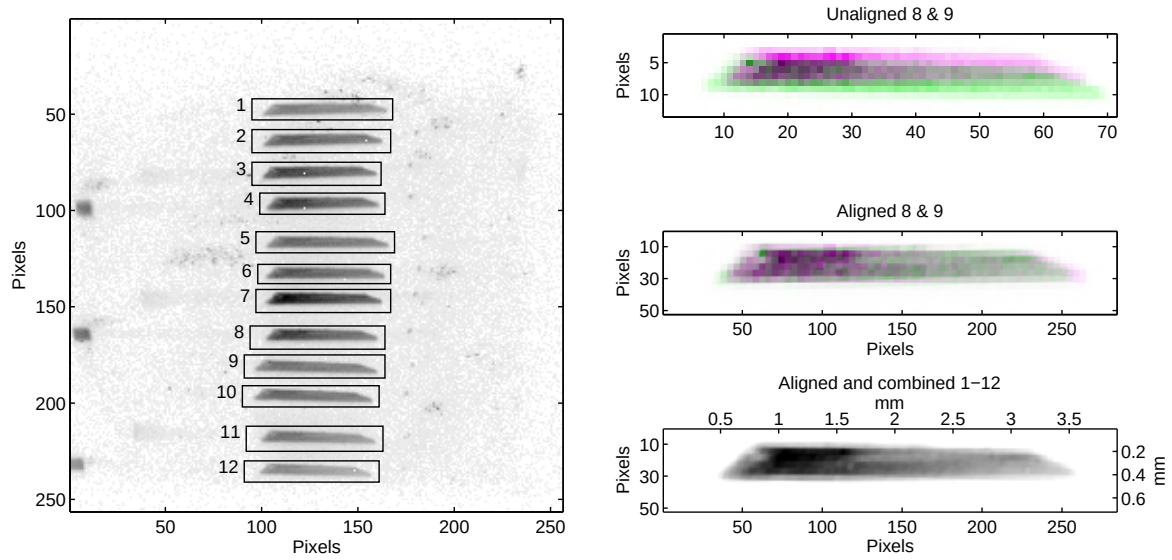

Figure 5: Imaging of a cinnamic acid crystal for paper **IV** using superresolution. Left: A detector image obtained by summing images of an energy scan across the elastic line. Right: The sub-images 8 and 9 (magenta and green, respectively) before and after alignment and interpolation. The interpolation grid has a number of pixels increased fourfold in both dimensions. The sub-image 8 is chosen as a reference for registration, to which all sub-images are aligned. The lowest panel illustrates the effect of aligning and combining all twelve sub-images.

4.3 Data analysis

In a typical measurement at ID20 the reflections from the analyzer crystals are aligned distinctively on the detector(s), see Fig. 5. Thus, by selecting regions of interest (ROIs) from the detector image, it is possible to discriminate the spectra from different analyzers, and to analyze each spectrum separately. This is necessary, because different analyzers pass slightly different energies, which needs to be accounted for in the energy-calibration. Also, as the analyzer crystals are positioned at different scattering angles, they record spectra with different momentum transfers, which can be desired to be resolved. A properly selected ROI enables to obtain spectra only from a desired volume of a sample and to avoid contributions from sample environment.

There are various ways to select the ROIs, and they are implemented in the program package presented in ref. [105]. Often the ROI selection is performed manually using an image obtained by an energy scan over the elastic line. For adequately uniform samples it is possible to detect the ROIs automatically based on an intensity threshold for pixels. The counts in each ROI are summed to result in spectra, which are then normalized to the flux of the incident beam. The spectra from individual analyzers are energy-calibrated to a common energy-transfer grid. If the desired momentum-transfer resolution allows, spectra from a group of analyzers may be averaged. Finally, the

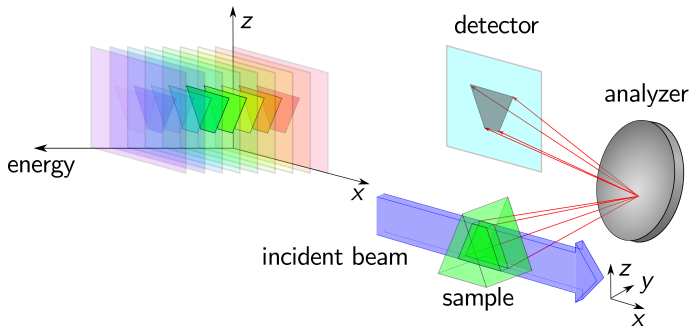

Figure 6: The principle of direct tomography imaging in 2D sectioning mode. An image of the x-ray illuminated volume of the sample is projected to the detector. Each pixel records an individual spectrum, and a hyperspectral data cube is formed.

spectra are corrected for the energy dependence of the x-ray absorption in air path, sample environment, and the sample itself.

In XRS, the spectra from specific core-electron excitations are of interest. In this case the parts of the spectra that originate from scattering from valence electrons or other, lower-lying, core electrons, is considered as background. Stray scattering, i.e., photons reaching detector but not via a reflection from analyzer crystals, may also contribute to the background. Sophisticated procedures to subtract the background and normalize the remaining spectrum to the dynamic structure factor on an absolute scale (1/eV) exist [105, 109, 110]. Normalization to the absolute scale is normally done using sum rules, if the spectra can be measured on a wide enough energy range [111]. Otherwise, if the interest is in relative comparison of spectra, the practice often is to normalize the spectra to a fixed area.

The detailed analysis procedures are presented in ref. [105] with a program package that can used to perform the analysis as well as to help to prepare for an experiment, e.g., by estimating count rates and signal-to-noise ratios.

4.4 Imaging at ID20

The imaging ability of ID20 can be utilized for many purposes. A straightforward one is to help the sample alignment and to exclude the signal from the sample environment. However, the most valuable feature of imaging exploits the spectral dimension of the recorded images, as it can provide contrast based on the chemical bonding. Similar imaging can be performed with x-ray and electron microscopies [37,112], but the NRIXS imaging technique, coined direct tomography [9], offers uniquely a contrast mechanism in three-dimensional imaging of macroscopically large samples (up to the mm-scale). Another application for the imaging is temperature probing of gaseous samples. The utilized imaging applications are presented along with the results of the experiments in Section 5.

Direct tomography yields, as any spectral imaging technique, data cubes that contain spectra as a function of spatial position and excitation energy. The data cubes can be obtained in two alternative ways. First is to use a tightly focused beam in both horizontal and vertical directions (e.g. 10 µm × 10 µm at ID20), and raster scan across the sample's directions y and z (see Fig. 6 for the coordinate system). The information of the position along the beam (x) is obtained from the detector images. It is also possible to image a two-dimensional section of a sample at once by using an x-ray beam unfocused in the z direction, obtaining an image slice in the xz plane from the detector images; the remaining information along the y direction is obtained by scanning the sample across the beam in this dimension.

The pixel-resolved spectra have only a fraction of the photon counts that the ROI-averaged spectra have, and their statistical accuracy is thus lower. To improve the statistics, individual hyperspectral images produced by each analyzer can be summed over. However, as the analyzer crystals have different angles of view to the sample, the images they produce can not be simply translated on top of each other and summed over. In principle, as the angular positions of the analyzers are known, it would be possible to apply a perspective correction to the individual images based on these positions. In practice, however, it is more straightforward to utilize automatic image registration [113], in which an image is transformed in such a way that it becomes aligned with another one and their intensities can be summed over. A sufficient transformation for the present case is an affine transformation, which combines translation, rotation, scaling, and shearing of images.

There is also a benefit in the different perspectives of the analyzers, as it enables a superresolution approach to improve the image resolution [114–116]. The image registration gives the transformation that aligns two low-resolution images as a whole, and generally this introduces a sub-pixel misalignment of the pixels (a point in the sample is pictured to different positions within the pixels of the images by different analyzers). If the low-resolution images with a sub-pixel misalignment are first interpolated to a finer resolution, and then merged, an image with improved resolution can be obtained. The superresolution method is demonstrated in Fig. 5.

4.5 Spectrum interpretation and decomposition

Different approaches can be used to interpret the spectral data to obtain the desired information. The information can be, for example, the presence of an element or a compound, the relative fractions of compounds, or even the orientation of certain chemical bonds [9]. Descriptive values of this information can be obtained from the spectrum by taking difference of intensities at appropriate energies, or by fitting with fingerprint spectra of known compounds (e.g., from the online database in ref. 117) or with component spectra given by spectral decomposition [37,112]. For spectral images,

the fitting yields weights for each pixel, which correspond to the relative fractions of the constituent components. In the case of three components, their fractions can be conveniently represented by colors. This is demonstrated for the case of dimerization of cinnamic acid (paper **IV**) in Fig. 9.

For gaining deeper information on the chemistry and on the neighborhood of the scattering site, the spectra need to be interpreted quantitatively. This is not always straightforward, since the relation between the molecular structure and the measured spectrum is complicated. As a first approach the spectra can be compared to reference spectra from known compounds. Also comparison of spectra measured from different phases, concentrations, or pressure and temperature conditions can be performed. This may allow identifying the changes in the chemical state of the probed element as a function of these parameters. However, often suitable reference spectra are not available. For gaining understanding on the structure-to-spectrum relation, computational simulations are often an irreplaceable tool, as they allow in-depth understanding of the spectral features. Several methods and program packages can be applied or have been developed for simulating NRIXS spectra for various cases, for example those described in refs. [17–21, 118, 119].

In paper **IV** a spectral decomposition analysis was performed on the measured time-resolved spectrum series using non-negative matrix factorization (NMF) [120,121]. NMF has been used for many purposes, such as image recognition [122], bioinformatics [123], and in other data mining applications [120]. In spectroscopy NMF has been used to analyze various kinds of data sets, e.g., pH- and concentration-varied spectrum series [124–128], and time-resolved spectra [129]. NMF and its variations have also been combined with hyperspectral imaging in x-ray microscopy [112, 130] and other fields [120]. A standard NMF analysis applies to two-dimensional data sets, but the method can be extended and generalized to multi-dimensional arrays, e.g., to analyze resonant emission spectra [120].

In NMF a non-negative data set matrix X is approximately factorized into non-negative matrices W and H, i.e. $X \approx WH$. In the case of a time-resolved spectrum series X, in which each individual spectrum is a sum of the component spectra of the constituent compounds weighted with their fractional abundances of each moment, W and H can be taken to represent the component spectra and their time-dependent weights. In NMF algorithms a required input parameter is the number of the components. It can be known beforehand or discovered by examining the spectral series, for example by observing isosbestic points.[5] It should be noted that the output matrices of NMF may suffer from rotational ambiguity, which has been discussed widely [120, 131–133]. The problem can be addressed in the case of spectral series by using appropriate initial guesses for the spectrum components and by critically inspecting the obtained results.

[5] An isosbestic point is a point in a spectral series that has a constant intensity, i.e., all the spectra cross in the isosbestic point.

The non-negativity constraint of NMF is in line with the physical interpretation of the output matrices as the component spectra and component weights. This is not the case for the results of spectral decomposition by widely used principal component analysis (PCA), as it considers the variance in a data set rather than linear combinations of the spectra of constituent compounds [112,129]. There exist also more specific methods for analyzing time-resolved data from chemical reactions, which may include reaction models already in the decomposition process [134]. Alternatively, as in paper **IV**, reaction kinetics parameters can be obtained from the time-dependent compound weights by fitting them with reaction models realized by solving differential equations describing the reaction in question [135, 136].

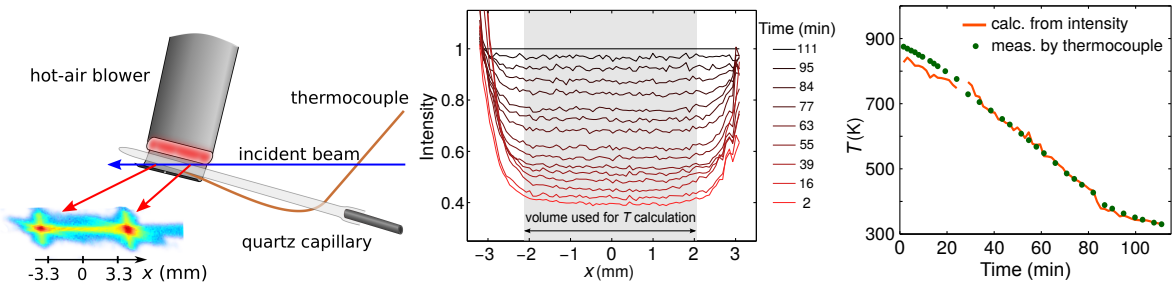

Figure 7: The setup used in the high-temperature measurements of gas samples and a demonstration of temperature probing by x-ray scattering. Left: The schematic figure of the setup, showing also the image formed on the detector by elastically scattered x-rays. Middle: Intensity of the scattered x-rays along the beam path normalized to that at the lowest temperature. Right: Temperature as a function of cooling time; calculated from elastic-line intensity and measured using a thermocouple.

5 Experiments and Results

This section summarizes the results of the studies in this thesis. Papers **I**–**III** are based on NRIXS experiments on gas-phase samples, which focused on the electronic excitation spectra and on the effects of molecular vibrations. Paper **IV** describes the first application of NRIXS for time-resolved imaging of a chemical reaction *in situ*.

Gas-phase experiments

Papers **I**–**III** were among the first studies of gaseous samples with NRIXS [11, 31, 33–36, 77, 78]. For these experiments a high-pressure sample cell with a sufficiently low x-ray attenuation was needed. In the experiment for papers **II**–**III** the cell was also required to tolerate high temperatures as also the effects of increased temperature were of interest. For these purposes a sample environment setup was assembled using a quartz capillary as the cell (Fig. 7). The setup allows to evacuate the cell using a membrane pump before filling it with the gaseous sample. The sample gas pressure was 50 bar in room temperature measurements and 40 bar in high-temperature measurements. Count rate was increased also by maximizing the probed gas volume by orienting the capillary nearly parallel to the x-ray beam.

In the high-temperature measurements of papers **II**–**III** the sample was heated with a hot-air blower to T=850 K. The temperature was measured with a thermocouple and determined also by using the temperature dependency of the intensity of elastically scattered x-rays. Since self-absorption in this case has a negligible effect and the gas can be considered as an ideal gas at a constant pressure, the intensity is proportional to number density of the gas and inversely proportional to its temperature. The intensity profile of the scattered x-rays along the incident beam path was obtained from the

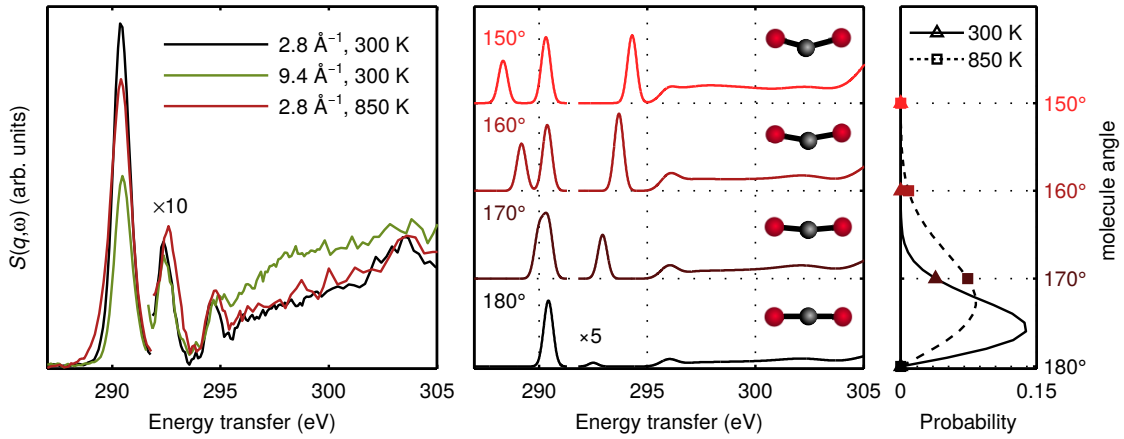

Figure 8: Results from the studies of the carbon core-electron excitations from CO_2. Left: The spectra measured with two values of momentum transfer and at two sample temperatures. Middle: The spectra calculated from molecular geometries with varied O–C–O bending angles. Right: The probability distributions of the geometries corresponding to the two temperatures.

detector images taken while cooling the sample to room temperature (middle panel of Fig. 7). The density ratio profiles yield inverse temperature ratio profiles, and using the room-temperature profile as a reference allowed to determine temperature of the gas. The temperature values obtained by both methods were in good agreement (right panel of Fig. 7). During the experiments the temperature profile of the heated gas was found to be flat at 850 K.

Paper I: Inelastic X-ray scattering and vibrational effects at the *K*-edges of gaseous N_2, N_2O, and CO_2

This paper presents a study on the core-electron excitations of several gas-phase molecules in ambient temperature. The simulation of the vibrational finestructure in the Franck–Condon approximation reproduces well the asymmetrical broadening of the electron excitation features observed in the experiment. The momentum transfer dependence of the spectrum shows the sensitivity to final states of different symmetries. The left panel of Fig. 8 presents the carbon core-electron excitation spectrum from room-temperature CO_2 measured at two momentum transfer values.

Paper II: Temperature dependence of CO_2 and N_2 core-electron excitation spectra at high pressure

This paper is a continuation for paper **I**. In this study the temperature dependence of the core-electron excitation spectra of CO_2 was investigated by measuring them at room temperature and at high temperature (850 K); see the left panel of Fig. 8

for the results of C K-edge. The spectra were simulated in a classical framework, in which the vibrational and temperature effects were accounted for by sampling molecular geometries corresponding to the sample temperatures and calculating the spectrum for each geometry. The results demonstrate that electronically forbidden excitations can become allowed when vibrations deviate the molecular geometry out of the equilibrium symmetry.

In the employed framework the temperature effects in the spectra arise from both the excitation intensity and energy dependency on the molecular geometry, and they are manifested as a continuous broadening of electronic excitation peaks. The experimentally observed temperature dependence is well reproduced by this straightforward simulation method. Most of the temperature dependency is explained by the bending mode, because it is the most easily excited vibrational mode.[6] The right panel of Fig. 8 shows the probability distributions along the bending coordinate in the two temperatures, and the middle panel shows the spectra calculated from selected molecular geometries. For example, the lowest-energy excitation peak at 290 eV is split to a lower and a higher energy part upon molecular bending, because in the linear molecule the corresponding final state is the degenerate $2\pi_u$ orbital, but in bent geometries the degeneracy is lifted. In turn, the second lowest energy excitation at 292 eV is forbidden in the linear geometry, but becomes allowed in bent geometries (its non-zero intensity in the 180°-spectrum is only due to contribution of non-dipole transitions). The feature gains weight upon bending of the molecule and shifts to higher energy.

Paper III: Interplay between Temperature-Activated Vibrations and Non-dipolar Effects in the Valence Excitations of the CO_2 Molecule

In this paper both the temperature and momentum transfer dependence of the valence electron excitation spectrum of CO_2 were studied. Following the simulation method of paper **II**, molecular geometries with varied bending angle were used to calculate the spectra, which were then weighted with the probability distribution corresponding to the sample temperatures. The momentum transfer dependence was accounted for by including both dipole and quadrupole transitions in the calculation. The results from experiment and simulation are in good agreement in both temperature and momentum transfer dependency. The intensity of some excitations is increased with an increasing momentum transfer, due to the increase of the weights of the quadrupole transition moments. Similar intensity variations occur also due to molecular bending. The simulation provided the symmetry assignment of all final states thus facilitating the interpretation of the effects as well as comparison to previous works on CO_2 valence exciation spectrum, for example refs. [50, 55, 71, 138–140].

[6] The wavenumbers of bending, and symmetric and antisymmetric stretching modes are 667 cm^{-1}, 1333 cm^{-1}, and 2349 cm^{-1}, respectively [137]. Thermal energy k_BT is 209 cm^{-1} and 591 cm^{-1} at 300 K and 850 K, respectively.

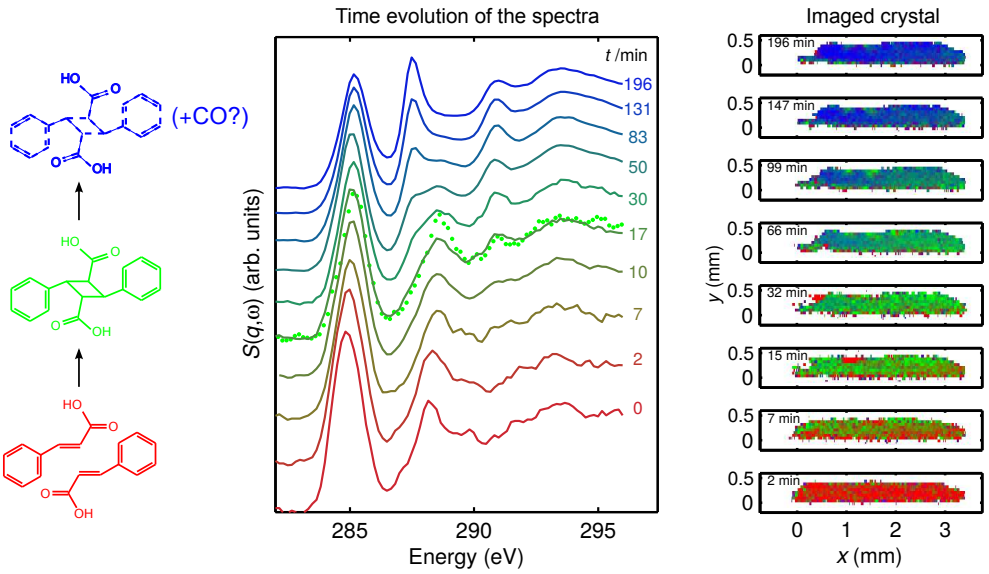

Figure 9: Following *in situ* chemical reactions with NRIXS. Left: The reaction scheme of the dimerization of α-trans-cinnamic acid to α-truxillic acid and a subsequent disintegration reaction, which with high probability produces CO fragments. Middle: The time-resolved carbon K-edge spectra. The spectrum of a reference α-truxillic acid sample is shown with green points. Right: The sample crystal imaged using spectroscopic contrast. Red, green, and blue channels correspond to the fitted weights of cinnamic acid, truxillic acid, and final products components, respectively.

Paper IV: X-ray induced dimerization of cinnamic acid: Time-resolved inelastic X-ray scattering study

In this paper the bulk sensitivity and imaging ability of NRIXS was employed for a time-resolved *in situ* study on the dimerization of α-trans-cinnamic acid [141, 142] (Fig. 9). It is a topochemical reaction [143, 144], governed by the initial crystal structure. The crystalline state imposes constraints to the pathways and products of chemical reactions, in contrast to disordered states. The dimerization of cinnamic acid is for long known to be induced by valence-electron excitations created by ultraviolet light illumination [141, 142]. However, this study showed that the dimerization is induced also by x-ray irradiation occurring during the NRIXS measurement.

The reaction was followed by consecutive measurements of carbon core-excitation spectrum (middle panel of Fig. 9). The time-evolution of the spectra shows that in ∼17 min of x-ray irradiation the spectrum from the cinnamic acid sample changes to resemble that of truxillic acid. The spectrum evolves further upon continued irradiation and a pronounced peak emerges suggesting a disintegration to take place. The energy of the new peak corresponds to that of the main peak of carbon monoxide spectrum [117, 145], suggesting CO to be a product of a subsequent disintegration process. The time-

resolved spectrum series was further analyzed by non-negative matrix factorization (Sec. 4.5), which enabled extracting the component spectra of the underlying pure compounds (cinnamic acid, truxillic acid, and final products from disintegration) and their time-dependent weights. An Avrami reaction model [135] fitted to the component weights suggests that the kinetics of the dimerization induced by x-rays differs from that induced by UV light [146, 147]. X-rays seem to produce a more homogeneous reaction, in comparison to the UV-induced dimerization, which has been suggested to be a combination of a homogeneous reaction and nuclei formation and their growth [146].

The reaction progress was also followed by the hyperspectral imaging method (Sec. 4.4). The superresolution method was utilized, and contrast was obtained by fitting the time-resolved hyperspectral images with the component spectra extracted by NMF. The resulting images are shown in the right panel of Fig. 9, where colors in each pixels correspond to the component weights.

6 Concluding Remarks

In this thesis non-resonant x-ray scattering applications were presented from an experimental perspective. The performed experiments have utilized the special abilities of NRIXS, namely the sensitivity to non-dipole excitations and the possibility to measure low-energy electronic excitations with high-energy x-rays. The large probing depth enabled bulk sensitivity and the use of sample environments for elevated pressures and temperatures. Novel data analysis methods as well as spectrum simulations were used in interpretation of the experimental data.

The studies on vibrational effects on electron excitation spectra have shown the significance of vibrations on spectral broadening and inspired practical approaches to simulate the temperature dependence of spectra. In the future, further insight to the vibrational effects could be obtained by studies of vibrationally resolved spectra corresponding to specific initial vibrational states. The presented experiments have also shown the capability of NRIXS for gaseous samples at readily varied pressures and temperatures above ambient conditions, thus paving the way to *in situ* studies on gas-phase reactions such as combustion. The study on the dimerization of cinnamic acid was the first time-resolved NRIXS experiment on a chemical reaction utilizing imaging.

The methods applied in this thesis for sample environments, data analysis, and imaging can help to envision future NRIXS studies on yet new areas. In particular, tomographic spectral imaging is foreseen to offer method for obtaining novel chemical information in many applications.

References

[1] W. Schülke, *Electron Dynamics by Inelastic X-ray Scattering* (Oxford University Press, 2007).

[2] U. Bergmann, P. Glatzel, and S. P. Cramer, *Bulk-sensitive XAS characterization of light elements: from X-ray Raman scattering to X-ray Raman spectroscopy*, Microchem. J. **71**, 221 (2002).

[3] K. Ishii, T. Tohyama, and J. Mizuki, *Inelastic X-ray Scattering Studies of Electronic Excitations*, J. Phys. Soc. Jpn. **82**, 021015 (2013).

[4] J.-P. Rueff and A. Shukla, *Inelastic x-ray scattering by electronic excitations under high pressure*, Rev. Mod. Phys. **82**, 847 (2010).

[5] S. Doniach, P. M. Platzman, and J. T. Yue, *X-Ray Raman Scattering in Metals*, Phys. Rev. B **4**, 3345 (1971).

[6] M. H. Krisch, F. Sette, C. Masciovecchio, and R. Verbeni, *Momentum Transfer Dependence of Inelastic X-Ray Scattering from the Li K Edge*, Phys. Rev. Lett. **78**, 2843 (1997).

[7] C. Sternemann, M. Volmer, J. Soininen, H. Nagasawa, M. Paulus, H. Enkisch, G. Schmidt, M. Tolan, and W. Schülke, *Momentum-transfer dependence of x-ray Raman scattering at the Be K-edge*, Phys. Rev. B **68**, 035111 (2003).

[8] R. Verbeni, T. Pylkkänen, S. Huotari, L. Simonelli, G. Vankó, K. Martel, C. Henriquet, and G. Monaco, *Multiple-element spectrometer for non-resonant inelastic X-ray spectroscopy of electronic excitations*, J. Synchrotron Radiat. **16**, 469 (2009).

[9] S. Huotari, T. Pylkkänen, R. Verbeni, G. Monaco, and K. Hämäläinen, *Direct tomography with chemical-bond contrast*, Nature Mater. **10**, 489 (2011).

[10] A. L. Kritcher, P. Neumayer, J. Castor, T. Döppner, R. W. Falcone, O. L. Landen, H. J. Lee, R. W. Lee, E. C. Morse, A. Ng, S. Pollaine, D. Price, and S. H. Glenzer, *Ultrafast X-ray Thomson Scattering of Shock-Compressed Matter*, Science **322**, 69 (2008).

[11] M. Minzer, J. A. Bradley, R. Musgrave, G. T. Seidler, and A. Skilton, *A pressure cell for nonresonant inelastic x-ray scattering studies of gas phases*, Rev. Sci. Instrum. **79**, 086101 (2008).

[12] J. Stöhr, *NEXAFS spectroscopy*, *Springer series in surface sciences* (Springer-Verlag, 1992).

[13] J. Als-Nielsen and D. McMorrow, *Elements of Modern X-ray Physics* (John Wiley & Sons, 2011).

[14] P. W. Atkins and R. S. Friedman, *Molecular quantum mechanics* (Oxford University Press, 2011).

[15] M. Cooper, *X-ray Compton scattering* (Oxford University Press, 2004).

[16] J. Hollas, *Modern Spectroscopy* (Wiley, 2004).

[17] A. Sakko, Ph.D. thesis, New computational approaches for inelastic x-ray scattering, University of Helsinki (2011).

[18] J. Lehtola, M. Hakala, A. Sakko, and K. Hämäläinen, *ERKALE - A Flexible Program Package for X-ray Properties of Atoms and Molecules*, J. Computat. Chem. **33**, 1572 (2012).

[19] J. Soininen, A. Ankudinov, and J. Rehr, *Inelastic scattering from core electrons: A multiple scattering approach*, Phys. Rev. B **72**, 045136 (2005).

[20] A. Castro, H. Appel, M. Oliveira, C. A. Rozzi, X. Andrade, F. Lorenzen, M. A. Marques, E. Gross, and A. Rubio, *Octopus: a tool for the application of time-dependent density functional theory*, Phys. Stat. Sol. B **243**, 2465 (2006).

[21] K. Gilmore, J. Vinson, E. Shirley, D. Prendergast, C. Pemmaraju, J. Kas, F. Vila, and J. Rehr, *Efficient implementation of core-excitation Bethe–Salpeter equation calculations*, Comput. Phys. Commun. (2015), doi:10.1016/j.cpc.2015.08.014.

[22] S. R. Shieh, I. Jarrige, M. Wu, N. Hiraoka, J. S. Tse, Z. Mi, L. Kaci, J.-Z. Jiang, and Y. Q. Cai, *Electronic structure of carbon dioxide under pressure and insights into the molecular-to-nonmolecular transition*, Proc. Natl. Acad. Sci. U.S.A. **110**, 18402 (2013).

[23] Ch. J. Sahle, C. Sternemann, C. Schmidt, S. Lehtola, S. Jahn, L. Simonelli, S. Huotari, M. Hakala, T. Pylkkänen, A. Nyrow, *et al.*, *Microscopic structure of water at elevated pressures and temperatures*, Proc. Natl. Acad. Sci. USA **110**, 6301 (2013).

[24] W. L. Mao, H.-k. Mao, P. J. Eng, T. P. Trainor, M. Newville, C.-C. Kao, D. L. Heinz, J. Shu, Y. Meng, and R. J. Hemley, *Bonding Changes in Compressed Superhard Graphite*, Science **302**, 425 (2003).

[25] Y. Meng, H.-K. Mao, P. J. Eng, T. P. Trainor, M. Newville, M. Y. Hu, C. Kao, J. Shu, D. Hausermann, and R. J. Hemley, *The formation of sp^3 bonding in compressed BN*, Nature Mater. **3**, 111 (2004).

[26] S. K. Lee, J.-F. Lin, Y. Q. Cai, N. Hiraoka, P. J. Eng, T. Okuchi, H.-k. Mao, Y. Meng, M. Y. Hu, P. Chow, J. Shu, B. Li, H. Fukui, B. H. Lee, H. N. Kim, and C.-S. Yoo, *X-ray Raman scattering study of $MgSiO_3$ glass at high pressure: Implication for triclustered $MgSiO_3$ melt in Earth's mantle*, Proc. Natl. Acad. Sci. USA **105**, 7925 (2008).

[27] S. K. Lee, P. J. Eng, H.-k. Mao, Y. Meng, M. Newville, M. Y. Hu, and J. Shu, *Probing of bonding changes in B_2O_3 glasses at high pressure with inelastic X-ray scattering*, Nature Mater. **4**, 851 (2005).

[28] F. de Groot and A. Kotani, *Core level spectroscopy of solids* (CRC Press, 2008).

[29] A. P. Hitchcock, *Inner shell excitation spectroscopy of molecules using inelastic electron scattering*, J. Electron. Spectrosc. Relat. Phenom. **112**, 9 (2000).

[30] B. Di Bartolo, *Spectroscopy and dynamics of collective excitations in solids* (Springer Science & Business Media, 1997), Vol. 356.

[31] J. A. Bradley, G. T. Seidler, G. Cooper, M. Vos, A. P. Hitchcock, A. P. Sorini, C. Schlimmer, and K. P. Nagle, *Comparative study of the valence electronic excitations of N_2 by inelastic x-ray and electron scattering*, Phys. Rev. Lett. **105**, 053202 (2010).

[32] J. A. Bradley, A. Sakko, G. T. Seidler, A. Rubio, M. Hakala, K. Hämäläinen, G. Cooper, A. P. Hitchcock, K. Schlimmer, and K. P. Nagle, *Reexamining the Lyman-Birge-Hopfield band of N_2*, Phys. Rev. A **84**, 022510 (2011).

[33] L. F. Zhu, W. Q. Xu, K. Yang, Z. Jiang, X. Kang, B. P. Xie, D. L. Feng, N. Hiraoka, and K. D. Tsuei, *Dynamic behavior of valence-shell excitations of atomic neon studied by high-resolution inelastic x-ray scattering*, Phys. Rev. A **85**, 030501 (2012).

[34] X. Kang, K. Yang, Y. W. Liu, W. Q. Xu, N. Hiraoka, K. D. Tsuei, P. F. Zhang, and L. F. Zhu, *Squared form factors of valence-shell excitations of atomic argon studied by high-resolution inelastic x-ray scattering*, Phys. Rev. A **86**, 022509 (2012).

[35] Y.-G. Peng, X. Kang, K. Yang, X.-L. Zhao, Y.-W. Liu, X.-X. Mei, W.-Q. Xu, N. Hiraoka, K.-D. Tsuei, and L.-F. Zhu, *Squared form factors of vibronic excitations in 12–13.3 eV of nitrogen studied by high-resolution inelastic x-ray scattering*, Phys. Rev. A **89**, 032512 (2014).

[36] D.-D. Ni, X. Kang, K. Yang, Y.-W. Liu, X.-X. Mei, X.-L. Zhao, L.-Q. Xu, N. Hiraoka, K.-D. Tsuei, and L.-F. Zhu, *Squared form factors for the $A^1\Pi$ and $B^1\Sigma^+$ vibronic bands of carbon monoxide studied by high-resolution inelastic x-ray scattering*, Phys. Rev. A **91**, 042501 (2015).

[37] R. Egerton, *Electron energy-loss spectroscopy in the electron microscope* (Springer Science & Business Media, 2011).

[38] T. Owen, *Fundamentals of UV-visible spectroscopy* (Hewlett Packard, 1996).

[39] B. Finlayson-Pitts and J. Pitts, *Chemistry of the Upper and Lower Atmosphere: Theory, Experiments, and Applications* (Elsevier Science, 1999).

[40] A. A. Viggiano, *Reexamination of ionospheric chemistry: high temperature kinetics, internal energy dependences, unusual isomers, and corrections*, Phys. Chem. Chem. Phys. **8**, 2557 (2006).

[41] P. Atkins and J. de Paula, *Atkins' Physical Chemistry* (Oxford University Press, 2010).

[42] T. Tanaka, C. Makochekanwa, H. Tanaka, M. Kitajima, M. Hoshino, Y. Tamenori, E. Kukk, X. J. Liu, G. Prümper, and K. Ueda, *Symmetry-Resolved Absorption Spectra of Vibrationally Excited CO_2 Molecules*, Phys. Rev. Lett. **95**, 203002 (2005).

[43] T. Tanaka, M. Hoshino, C. Makochekanwa, M. Kitajima, G. Prümper, X. Liu, T. Lischke, K. Nakagawa, H. Kato, Y. Tamenori, J. Harries, H. Tanaka, and K. Ueda, *Angle-resolved ion yield spectroscopy for the 1s3π excited states in hot N_2O molecules*, Chem. Phys. Lett. **428**, 34 (2006).

[44] T. Tanaka, M. Hoshino, H. Kato, M. Ehara, N. Yamada, R. Fukuda, H. Nakatsuji, Y. Tamenori, J. R. Harries, G. Prümper, H. Tanaka, and K. Ueda, *Vibration-induced suppression of valence-rydberg mixing in the O 1s→nsσ rydberg series in N_2O*, Phys. Rev. A **77**, 012709 (2008).

[45] T. Tanaka, M. Hoshino, R. R. Lucchese, Y. Tamenori, H. Kato, H. Tanaka, and K. Ueda, *Bending-induced diminution of shape resonances in the core-level absorption region of hot CO_2 and N_2O*, New J. Phys. **12**, 123017 (2010).

[46] F.-T. Chau, J. M. Dyke, E. P.-F. Lee, and D.-C. Wang, *Franck–Condon analysis of photoelectron and electronic spectra of small molecules*, J. Electron. Spectrosc. Relat. Phenom. **97**, 33 (1998).

[47] F. Santoro, A. Lami, R. Improta, J. Bloino, and V. Barone, *Effective method for the computation of optical spectra of large molecules at finite temperature including the Duschinsky and Herzberg–Teller effect: The Q_x band of porphyrin as a case study*, J. Chem. Phys. **128**, 224311 (2008).

[48] C. P. Schwartz, J. S. Uejio, R. J. Saykally, and D. Prendergast, *On the importance of nuclear quantum motions in near edge x-ray absorption fine structure spectroscopy of molecules*, J. Chem. Phys. **130**, 184109 (2009).

[49] S. Y. Grebenshchikov, *Photodissociation of carbon dioxide in singlet valence electronic states. I. Six multiply intersecting ab initio potential energy surfaces*, J. Chem. Phys **138**, 224106 (2013).

[50] S. Y. Grebenshchikov, *Photodissociation of carbon dioxide in singlet valence electronic states. II. Five state absorption spectrum and vibronic assignment*, J. Chem. Phys **138**, 224107 (2013).

[51] J. S. Uejio, C. P. Schwartz, R. J. Saykally, and D. Prendergast, *Effects of vibrational motion on core-level spectra of prototype organic molecules*, Chem. Phys. Lett. **467**, 195 (2008).

[52] S. Fatehi, C. P. Schwartz, R. J. Saykally, and D. Prendergast, *Nuclear quantum effects in the structure and lineshapes of the N_2 near-edge x-ray absorption fine structure spectrum*, J. Chem. Phys. **132**, 094302 (2010).

[53] J. Thomas and W. Thomas, *Principles and Practice of Heterogeneous Catalysis* (Wiley, 1996).

[54] G. Côme, *Gas-Phase Thermal Reactions: Chemical Engineering Kinetics* (Springer, 2001).

[55] Venot, O., Fray, N., Bénilan, Y., Gazeau, M.-C., Hébrard, E., Larcher, G., Schwell, M., Dobrijevic, M., and Selsis, F., *High-temperature measurements of VUV-absorption cross sections of CO_2 and their application to exoplanets*, A&A **551**, A131 (2013).

[56] J. A. Schmidt, M. S. Johnson, and R. Schinke, *Carbon dioxide photolysis from 150 to 210 nm: Singlet and triplet channel dynamics, UV-spectrum, and isotope effects*, Proc. Natl. Acad. Sci. USA **110**, 17691 (2013).

[57] M. Kneba and J. Wolfrum, *Bimolecular Reactions of Vibrationally Excited Molecules*, Annu. Rev. Phys. Chem. **31**, 47 (1980).

[58] F. F. Crim, *Chemical dynamics of vibrationally excited molecules: Controlling reactions in gases and on surfaces*, Proc. Natl. Acad. Sci. USA **105**, 12654 (2008).

[59] Y. Ma, C. T. Chen, G. Meigs, K. Randall, and F. Sette, *High-resolution K-shell photoabsorption measurements of simple molecules*, Phys. Rev. A **44**, 1848 (1991).

[60] E. Kukk, J. D. Bozek, and N. Berrah, *Photoexcitation and Auger decay of the Renner-Teller split C 1s-1 π_u^* state in* CO_2, Phys. Rev. A **62**, 032708 (2000).

[61] H. Yoshida, K. Nobusada, K. Okada, S. Tanimoto, N. Saito, A. De Fanis, and K. Ueda, *Symmetry-Resolved Vibrational Spectroscopy for the C $1s^{-1}2\pi_u$ Renner-Teller Pair States in CO_2*, Phys. Rev. Lett. **88**, 083001 (2002).

[62] J. Adachi, N. Kosugi, E. Shigemasa, and A. Yagishita, *Vibronic Couplings in the C 1s $\rightarrow$ $ns\sigma_g$ Rydberg Excited States of CO_2*, J. Phys. Chem. **100**, 19783 (1996).

[63] K. Okada, H. Yoshida, Y. Senba, K. Kamimori, Y. Tamenori, H. Ohashi, K. Ueda, and T. Ibuki, *Angle-resolved ion-yield measurements of CO_2 in the O 1s to Rydberg excitation region*, Phys. Rev. A **66**, 032503 (2002).

[64] C. T. Chen, Y. Ma, and F. Sette, *K-shell photoabsorption of the N_2 molecule*, Phys. Rev. A **40**, 6737 (1989).

[65] V. Sivkov, A. Vinogradov, S. Nekipelov, D. Sivkov, D. Vyalykh, and S. Molodtsov, *Oscillator strengths of the vibrational and Rydberg transitions in the 1s absorption spectrum of a nitrogen molecule*, Opt. Spectrosc. **102**, 367 (2007).

[66] M. Kato, Y. Morishita, M. Oura, H. Yamaoka, Y. Tamenori, K. Okada, T. Matsudo, T. Gejo, I. Suzuki, and N. Saito, *Absolute photoionization cross sections with ultra-high energy resolution for Ar, Kr, Xe and N_2 in inner-shell ionization regions*, J. Electron. Spectrosc. Relat. Phenom. **160**, 39 (2007).

[67] K. Prince, M. Vondráček, J. Karvonen, M. Coreno, R. Camilloni, L. Avaldi, and M. De Simone, *A critical comparison of selected 1s and 2p core hole widths*, J. Electron. Spectrosc. Relat. Phenom. **101**, 141 (1999).

[68] B. Yates, Y. Hu, K. Tan, G. Retzlaff, R. Cavell, T. Sham, and G. Bancroft, *First results from the Canadian SGM beamline at SRC*, J. Synchrotron Rad. **7**, 296 (2000).

[69] E. C. Inn, K. Watanabe, and M. Zelikoff, *Absorption coefficients of gases in the vacuum ultraviolet. Part III. CO_2*, J. Chem. Phys. **21**, 1648 (1953).

[70] W. Chan, G. Cooper, and C. Brion, *The electronic spectrum of carbon dioxide. Discrete and continuum photoabsorption oscillator strengths (6–203 eV)*, Chem. Phys. **178**, 401 (1993).

[71] K. Yoshino, J. Esmond, Y. Sun, W. Parkinson, K. Ito, and T. Matsui, *Absorption cross section measurements of carbon dioxide in the wavelength region 118.7–175.5 nm and the temperature dependence*, J. Quant. Spectrosc. Radiat. Transfer **55**, 53 (1996).

[72] W. Parkinson, J. Rufus, and K. Yoshino, *Absolute absorption cross section measurements of CO_2 in the wavelength region 163–200 nm and the temperature dependence*, Chem. Phys. **290**, 251 (2003).

[73] L. Archer, G. Stark, P. Smith, J. Lyons, N. de Oliveira, L. Nahon, D. Joyeux, and D. Blackie, *Room temperature photoabsorption cross section measurements of CO_2 between 91,000 and 115,000 cm^{-1}*, J. Quant. Spectrosc. Radiat. Transfer **117**, 88 (2013).

[74] E. N. Lassettre and M. E. Krasnow, *Collision Cross-Section Study of Two Transitions in Nitrogen*, J. Chem. Phys. **40**, 1248 (1964).

[75] A. Skerbele and E. N. Lassettre, *Absolute Electron Collision Cross Sections for Two Forbidden Transitions in Nitrogen at Kinetic Energies of 300–500 eV*, J. Chem. Phys. **53**, 3806 (1970).

[76] M. Brunger and P. Teubner, *Differential cross sections for electron-impact excitation of the electronic states of N_2*, Phys. Rev. A **41**, 1413 (1990).

[77] B. P. Xie, L. F. Zhu, K. Yang, B. Zhou, N. Hiraoka, Y. Q. Cai, Y. Yao, C. Q. Wu, E. L. Wang, and D. L. Feng, *Inelastic x-ray scattering study of the state-resolved differential cross section of Compton excitations in helium atoms*, Phys. Rev. A **82**, 032501 (2010).

[78] L. F. Zhu, L. S. Wang, B. P. Xie, K. Yang, N. Hiraoka, Y. Q. Cai, and D. L. Feng, *Inelastic x-ray scattering study on the single excitations of helium*, J. Phys. B **44**, 025203 (2011).

[79] U. Hergenhahn, *Vibrational structure in inner shell photoionization of molecules*, J. Phys. B **37**, R89 (2004).

[80] T. Azumi and K. Matsuzaki, *What does the term "vibronic coupling" mean?*, Photochemistry and Photobiology **25**, 315 (1977).

[81] O'Donnell J.H. and Sangster D.F., *Principles of Radiation Chemistry* (Arnold, 1970).

[82] R. J. Woods and A. K. Pikaev, *Applied radiation chemistry: radiation processing* (John Wiley & Sons, 1994).

[83] R. B. Ravelli and E. F. Garman, *Radiation damage in macromolecular cryocrystallography*, Curr. Opin. Struct. Biol. **16**, 624 (2006).

[84] J. M. Holton, *A beginner's guide to radiation damage*, J. Synchrotron Rad. **16**, 133 (2009).

[85] E. F. Garman, *Radiation damage in macromolecular crystallography: what is it and why should we care?*, Acta Crystallogr. Sect. D-Biol. Crystallogr. **66**, 339 (2010).

[86] A. Meents, S. Gutmann, A. Wagner, and C. Schulze-Briese, *Origin and temperature dependence of radiation damage in biological samples at cryogenic temperatures*, Proc. Natl. Acad. Sci. U.S.A. **107**, 1094 (2010).

[87] A. Gianoncelli, L. Vaccari, G. Kourousias, D. Cassese, D. Bedolla, S. Kenig, P. Storici, M. Lazzarino, and M. Kiskinova, *Soft X-Ray Microscopy Radiation Damage On Fixed Cells Investigated With Synchrotron Radiation FTIR Microscopy*, Scientific Reports **5**, (2015), doi: 10.1038/srep10250.

[88] M. R. Howells, T. Beetz, H. N. Chapman, C. Cui, J. Holton, C. Jacobsen, J. Kirz, E. Lima, S. Marchesini, H. Miao, *et al.*, *An assessment of the resolution limitation due to radiation-damage in x-ray diffraction microscopy*, J. Electron. Spectrosc. Relat. Phenom. **170**, 4 (2009).

[89] A. J. Swallow, *Radiation Chemistry of Organic Compounds: International Series of Monographs on Radiation Effects* (Pergamon Press, 1960), Vol. 2.

[90] D. T. Ha, Y. Wang, M. Alcamí, E. Itälä, K. Kooser, S. Urpelainen, M. A. Huels, E. Kukk, and F. Martín, *Fragmentation Dynamics of Doubly Charged Methionine in the Gas Phase*, J. Phys. Chem. A **118**, 1374 (2014).

[91] J. Laksman, K. Kooser, H. Levola, E. Itälä, D. Ha, E. Rachlew, and E. Kukk, *Dissociation Pathways in the Cysteine Dication after Site-Selective Core Ionization*, J. Phys. Chem. B **118**, 11688 (2014).

[92] N. Carron, *An Introduction to the Passage of Energetic Particles through Matter* (Taylor & Francis, 2006).

[93] R. Bruckner, *Organic mechanisms* (Springer, 2010), pp. 418–419.

[94] G. Choppin, J. Liljenzin, and J. Rydberg, *Radiochemistry and Nuclear Chemistry* (Butterworth-Heinemann, 1995).

[95] S. Ohba and Y. Ito, *Single-crystal-to-single-crystal photodimerization of 4-chlorocinnamoyl-O,O'-dimethyldopamine*, Acta Crystallogr. Sect. B-Struct. Sci. **59**, 149 (2003).

[96] K. Tashiro, A. N. Zadorin, S. Saragai, T. Kamae, A. Matsumoto, K. Yokoi, and S. Aoki, *Structure Analysis of Monomer and Polymer Crystals in the Photoinduced Solid-State Polymerization Reaction of Diethyl cis,cis-Muconate*, Macromolecules **32**, 7946 (1999).

[97] A. Mori, N. Kato, H. Takeshita, Y. Kurahashi, and M. Ito, *X-Ray-induced retro [2 + 2] cycloaddition of a syn-tricyclo[4.2.0.0 ^{2,5}]octane derivative to a cis,cis-cycloocta-1,5-diene derivative within a single crystal lattice*, J. Chem. Soc., Chem. Commun. 869 (1994).

[98] A. E. Cohen, S. M. Soltis, A. González, L. Aguila, R. Alonso-Mori, C. O. Barnes, E. L. Baxter, W. Brehmer, A. S. Brewster, A. T. Brunger, *et al.*, *Goniometer-based femtosecond crystallography with X-ray free electron lasers*, Proc. Natl. Acad. Sci. USA **111**, 17122 (2014).

[99] M. Nagasaka, T. Hatsui, T. Horigome, Y. Hamamura, and N. Kosugi, *Development of a liquid flow cell to measure soft x-ray absorption in transmission mode: a test for liquid water*, J. Electron. Spectrosc. Relat. Phenom. **177**, 130 (2010).

[100] S. Schreck, G. Gavrila, C. Weniger, and P. Wernet, *A sample holder for soft x-ray absorption spectroscopy of liquids in transmission mode*, Rev. Sci. Instrum. **82**, 103101 (2011).

[101] A. Lindblad, S. Svensson, and K. Tiedtke, *A compendium on beam transport and beam diagnostic methods for Free Electron Lasers* (Deutsches Elektronen-Synchrotron DESY, 2011).

[102] Y. Q. Cai, P. Chow, C. C. Chen, H. Ishii, K. L. Tsang, C. C. Kao, K. S. Liang, and C. T. Chen, *Optical design and performance of the Taiwan inelastic x-ray scattering beamline (BL12XU) at Spring-8*, AIP Conf. Proc. **705**, 340 (2004).

[103] T. T. Fister, G. T. Seidler, L. Wharton, A. R. Battle, T. B. Ellis, J. O. Cross, A. T. Macrander, W. T. Elam, T. A. Tyson, and Q. Qian, *Multielement spectrometer for efficient measurement of the momentum transfer dependence of inelastic x-ray scattering*, Rev. Sci. Instrum. **77**, 063901 (2006).

[104] J. Campbell and T. Papp, *Widths of the atomic K–N7 levels*, Atomic Data and Nuclear Data Tables **77**, 1 (2001).

[105] Ch. J. Sahle, A. Mirone, J. Niskanen, J. Inkinen, M. Krisch, and S. Huotari, *Planning, performing and analyzing X-ray Raman scattering experiments*, J. Synchrotron Rad. **22**, 400 (2015).

[106] H. Winick, *Synchrotron radiation sources: a primer* (World Scientific, 1995), Vol. 1.

[107] A.-P. Honkanen, R. Verbeni, L. Simonelli, M. Moretti Sala, G. Monaco, and S. Huotari, *Study on the reflectivity properties of spherically bent analyser crystals*, J. Synchrotron Rad. **21**, 104 (2014).

[108] X. Llopart, M. Campbell, R. Dinapoli, D. S. Segundo, and E. Pernigotti, *Medipix2: a 64-k pixel readout chip with 55-μm square elements working in single photon counting mode*, IEEE Transactions on Nuclear Science **49**, 2279 (2002).

[109] S. Huotari, T. Pylkkänen, J. A. Soininen, J. J. Kas, K. Hämäläinen, and G. Monaco, *X-ray-Raman-scattering-based EXAFS beyond the dipole limit*, J. Synchrotron Rad. **19**, 106 (2011).

[110] H. Sternemann, C. Sternemann, G. T. Seidler, T. T. Fister, A. Sakko, and M. Tolan, *An extraction algorithm for core-level excitations in non-resonant inelastic X-ray scattering spectra*, J. Synchrotron Rad. **15**, 162 (2008).

[111] P. Eisenberger and P. M. Platzman, *Compton Scattering of X Rays from Bound Electrons*, Phys. Rev. A **2**, 415 (1970).

[112] J. Sedlmair, *Soft x-ray spectromicroscopy of environmental and biological samples* (Universitätsverlag Göttingen, 2011), Vol. 7.

[113] R. C. Gonzales, *Digital image processing using Matlab* (Tata McGraw-Hill Education, YEAR).

[114] S. Baker and T. Kanade, *Limits on super-resolution and how to break them*, IEEE Trans. Pattern Anal. Mach. Intell. **24**, 1167 (2002).

[115] S. C. Park, M. K. Park, and M. G. Kang, *Super-resolution image reconstruction: a technical overview*, IEEE Signal Proc. Mag. **20**, 21 (2003).

[116] S. Farsiu, D. Robinson, M. Elad, and P. Milanfar, *Advances and challenges in super-resolution*, Int. J. Imag. Syst. Tech. **14**, 47 (2004).

[117] A. Hitchcock and D. Mancini, Gas Phase Core Excitation Database, http://unicorn.mcmaster.ca/corex/cedb-title.html, 1980, (retrieved 16th December 2014).

[118] J. Lehtola, ERKALE, http://erkale.googlecode.com, 2012.

[119] A. Sakko, M. Hakala, J. Soininen, and K. Hämäläinen, *Density functional study of x-ray Raman scattering from aromatic hydrocarbons and polyfluorene*, Phys. Rev. B **76**, 205115 (2007).

[120] A. Cichocki, R. Zdunek, A. H. Phan, and S. Amari, *Non-negative matrix and tensor factorizations: applications to exploratory multi-way data analysis and blind source separation.* (Wiley Publishing, 2009).

[121] Y.-X. Wang and Y.-J. Zhang, *Nonnegative matrix factorization: A comprehensive review*, IEEE T. Knowl. Data En. **25**, 1336 (2013).

[122] D. D. Lee and H. S. Seung, *Learning the parts of objects by non-negative matrix factorization*, Nature **401**, 788 (1999).

[123] Li Y and Ngom A., *The non-negative matrix factorization toolbox for biological data mining.*, Source Code Biol. Med. **8**, (2013).

[124] S. K. Srivastava, S. Niebling, B. Küstner, P. R. Wich, C. Schmuck, and S. Schlücker, *Characterization of guanidiniocarbonyl pyrroles in water by pH-dependent UV Raman spectroscopy and component analysis*, Phys. Chem. Chem. Phys. **10**, 6770 (2008).

[125] S. Niebling, S. K. Srivastava, C. Herrmann, P. R. Wich, C. Schmuck, and S. Schlücker, *Site-specific pK_a determination of the carboxylate-binding subunit in artificial peptide receptors*, Chem. Commun. **46**, 2133 (2010).

[126] S. Niebling, H. Y. Kuchelmeister, C. Schmuck, and S. Schlücker, *Quantitative, label-free and site-specific monitoring of molecular recognition: a multivariate resonance Raman approach*, Chem. Commun. **47**, 568 (2011).

[127] W. Xie, C. Herrmann, K. Kömpe, M. Haase, and S. Schlücker, *Synthesis of Bifunctional Au/Pt/Au Core/Shell Nanoraspberries for in situ SERS Monitoring of Platinum-Catalyzed Reactions*, J. Am. Chem. Soc. **133**, 19302 (2011).

[128] I. Kopriva, I. Jerić, and A. Cichocki, *Blind decomposition of infrared spectra using flexible component analysis*, Chemometr. Intell. Lab. **97**, 170 (2009).

[129] P. Liu, X. Zhou, Y. Li, M. Li, D. Yu, and J. Liu, *The application of principal component analysis and non-negative matrix factorization to analyze time-resolved optical waveguide absorption spectroscopy data*, Anal. Methods **5**, 4454 (2013).

[130] R. Mak, M. Lerotic, H. Fleckenstein, S. Vogt, S. M. Wild, S. Leyffer, Y. Sheynkin, and C. Jacobsen, *Non-negative matrix analysis for effective feature extraction in X-ray spectromicroscopy*, Farad. Discuss. **171**, 357 (2014).

[131] H. Laurberg, M. G. Christensen, M. D. Plumbley, L. K. Hansen, and S. H. Jensen, *Theorems on positive data: On the uniqueness of NMF*, Comput. Intell. Neurosci. **2008**, (2008).

[132] R. Schachtner, G. Pöppel, and E. W. Lang, *Towards unique solutions of non-negative matrix factorization problems by a determinant criterion*, Digit. Signal Process. **21**, 528 (2011).

[133] N. Gillis, *Sparse and unique nonnegative matrix factorization through data preprocessing*, J. Mach. Learn. Res. **13**, 3349 (2012).

[134] A. de Juan and R. Tauler, *Multivariate Curve Resolution (MCR) from 2000: Progress in Concepts and Applications*, Crit. Rev. Anal. Chem. **36**, 163 (2006).

[135] A. Khawam and D. R. Flanagan, *Solid-State Kinetic Models: Basics and Mathematical Fundamentals*, J. Phys. Chem. B **110**, 17315 (2006).

[136] G. Puxty, M. Maeder, and K. Hungerbühler, *Tutorial on the fitting of kinetics models to multivariate spectroscopic measurements with non-linear least-squares regression*, Chemometr. Intell. Lab. **81**, 149 (2006).

[137] T. Shimanouchi, in *NIST Chemistry WebBook, NIST Standard Reference Database Number 69*, edited by E. P. Linstrom and W. Mallard (National Institute of Standards and Technology, 1972), Chap. Molecular Vibrational Frequencies, http://webbook.nist.gov.

[138] B. Lewis and J. Carver, *Temperature dependence of the carbon dioxide photoabsorption cross section between 1200 and 1970 Å*, J. Quant. Spectrosc. Radiat. Transfer **30**, 297 (1983).

[139] C. Schulz, J. Koch, D. Davidson, J. Jeffries, and R. Hanson, *Ultraviolet absorption spectra of shock-heated carbon dioxide and water between 900 and 3050 K*, Chem. Phys. Lett. **355**, 82 (2002).

[140] R. J. Jensen, R. D. Guettler, and J. L. Lyman, *The ultraviolet absorption spectrum of hot carbon dioxide*, Chem. Phys. Lett. **277**, 356 (1997).

[141] M. D. Cohen, G. M. J. Schmidt, and F. I. Sonntag, *384. Topochemistry. Part II. The photochemistry of trans-cinnamic acids*, J. Chem. Soc. 2000 (1964).

[142] V. Enkelmann, G. Wegner, K. Novak, and K. B. Wagener, *Single-crystal-to-single-crystal photodimerization of cinnamic acid*, J. Am. Chem. Soc. **115**, 10390 (1993).

[143] K. Biradha and R. Santra, *Crystal engineering of topochemical solid state reactions*, Chem. Soc. Rev. **42**, 950 (2013).

[144] I. Jahnke, Eike and Lieberwirth, *Topochemical Polymerization in Supramolecular Polymers of Oligopeptide-Functionalized Diacetylenes*, Angew. Chem. Int. Ed. **45**, 5383 (2006).

[145] A. Hitchcock and C. Brion, *K-shell excitation spectra of CO, N_2 and O_2*, J. Electron. Spectrosc. Relat. Phenom. **18**, 1 (1980).

[146] J. B. Benedict and P. Coppens, *Kinetics of the Single-Crystal to Single-Crystal Two-Photon Photodimerization of α-trans-Cinnamic Acid to α-Truxillic Acid*, J. Phys. Chem. A **113**, 3116 (2009).

[147] M. Bertmer, R. C. Nieuwendaal, A. B. Barnes, and S. E. Hayes, *Solid-State Photodimerization Kinetics of α-trans-Cinnamic Acid to α-Truxillic Acid Studied via Solid-State NMR*, J. Phys. Chem. B **110**, 6270 (2006).